

Contents lists available at ScienceDirect

Journal of Energy Chemistry



http://www.journals.elsevier.com/

journal homepage: www.elsevier.com/locate/jechem

N-doped porous carbon nanofibers sheathed pumpkin-like Si/C composites as free-standing anodes for lithium-ion batteries

Yanfei Zeng^a, Yudai Huang^{a,*}, Niantao Liu^a, Xingchao Wang^a, Yue Zhang^a, Yong Guo^a, Hong-Hui Wu^c, Huixin Chen^e, Xincun Tang^d, Qiaobao Zhang^{b,*}

ARTICLE INFO

Article history: Received 5 May 2020 Revised 29 May 2020 Accepted 8 June 2020 Available online 25 June 2020

Keywords: Pumpkin-like silicon/carbon composites N-doped porous carbon nanofibers Free-standing anode Lithium-ion batteries

ABSTRACT

Dramatic capacity fading and poor rate performance are two main obstacles that severely hamper the widespread application of the Si anode owing to its large volume variation during cycling and low intrinsic electrical conductivity. To mitigate these issues, free-standing N-doped porous carbon nanofibers sheathed pumpkin-like Si/C composites (Si/C-ZIF-8/CNFs) are designed and synthesized by electrospinning and carbonization methods, which present greatly enhanced electrochemical properties for lithium-ion battery anodes. This particular structure alleviates the volume variation, promotes the formation of stable solid electrolyte interphase (SEI) film, and improves the electrical conductivity. As a result, the as-obtained free-standing Si/C-ZIF-8/CNFs electrode delivers a high reversible capacity of 945.5 mA h g⁻¹ at 0.2 A g⁻¹ with a capacity retention of 64% for 150 cycles, and exhibits a reversible capacity of 538.6 mA h g⁻¹ at 0.5 A g⁻¹ over 500 cycles. Moreover, the full cell composed of a free-standing Si/C-ZIF-8/CNFs anode and commercial LiNi_{1/3}Co_{1/3}Mn_{1/3}O₂ (NCM) cathode shows a capacity of 63.4 mA h g⁻¹ after 100 cycles at 0.2 C, which corresponds to a capacity retention of 60%. This rational design could provide a new path for the development of high-performance Si-based anodes.

© 2020 Science Press and Dalian Institute of Chemical Physics, Chinese Academy of Sciences. Published by ELSEVIER B.V. and Science Press. All rights reserved.

1. Introduction

To date, lithium-ion batteries (LIBs) have been widely used in advanced mobile electric vehicles (EVs) and portable electronics because of their high energy density and long lifecycle [1–10]. However, the capacity of traditional graphite anodes (372 mA h g $^{-1}$) cannot meet the requirement of LIBs for higher energy density [11,12]. Among the existing candidates, Si anodes have been regarded as the most promising alternative to graphite for LIBs ascribing to the abundant natural resources, low discharge potential (~0.4 V versus Li/Li $^+$), and high theoretical specific capacity (~3579 mA h g $^{-1}$ Li $_{15}$ Si $_4$) [13–15]. However, Si anodes suffer from several challenges, including severe volume change (>270%) during

the Li⁺ ion insertion/extraction process, excessive accumulation of solid electrolyte interphase (SEI) during cycling, and low intrinsic electronic conductivity, resulting in rapid capacity fading upon cycling and poor rate capability [16–18]. Recent works attempted to use Si in the design of nanostructures, such as nanorods [19], nanowires [20], nanotubes [21], nanoporous structures [22], and nanosheets [23], to alleviate its severe volume change during cycling. However, the electrochemical performance has not been significantly improved due to the unstable SEI formation and intrinsically low conductivity. To mitigate these problems, the strategy is to introduce conductive carbonaceous material to the Si anode, which can notably promote favorable SEI formation and enhance the conductivity of Si [24,25]. As a result, the electrochemical performance of the Si anode is improved. However, the C shell still breaks over time due to limited space for volume variation during the charge-discharge process. Therefore, developing a strategy to create enough voids between the Si core and

^a Key Laboratory of Energy Materials Chemistry, Ministry of Education, Key Laboratory of Advanced Functional Materials, Autonomous Region, Institute of Applied Chemistry, College of Chemistry, Xinjiang University, Urumqi 830046, Xinjiang, China

^b Department of Materials Science and Engineering, College of Materials, Xiamen University, Xiamen 361005, Fujian, China

^c Beijing Advanced Innovation Center for Materials Genome Engineering, School of Materials Science and Engineering, University of Science and Technology Beijing, Beijing 100083, China

^d School of Chemistry and Chemical Engineering, Central South University, Changsha 410083, Hunan, China

^e Xiamen Institute of Rare Earth Materials, Haixi Institutes, Chinese Academy of Sciences, Xiamen 361024, Fujian, China

^{*} Corresponding authors.

E-mail addresses: huangyd@xju.edu.cn (Y. Huang), zhangqiaobao@xmu.edu.cn (Q. Zhang).

the C shell is of great importance to alleviate the volume expansion.

Yolk-shell structure has been demonstrated as an important structure in many research fields, such as catalysis, energy storage, and conversion [26]. Particularly, the hollow shell is an effective way to accommodate the volume expansion of Si. The pumpkinlike structure is similar to the structure of multi-core yolk-shell, in which Si nanoparticles are embedded in a hollow C shell. Compared with the single-core yolk-shell structure, pumpkin-like material contains larger spaces to allow the volume expansion of Si [27]. Metal-organic frameworks (MOFs) are good templates for the synthesis of yolk-shell structure, which consist of Li⁺ and organic ligands. MOFs have been widely studied in LIBs owing to their high specific areas and controllable synthesis [28]. Among various MOFs, zeolitic imidazolate framework-8 (ZIF-8) is an ideal choice for volk-shell structure because of its exceptional thermal/chemical stability [29]. In addition, it also can be easily etched in a solution and removed during the annealing process. These merits make ZIF-8 an ideal template for creating a void to buffer the voltime expansion of Si.

Furthermore, Si/C based electrodes are usually assembled by casting slurries, which easily delaminate the active material from the electrode during the cycling process. Moreover, the utilization of electrochemically inactive binders and additives results in a decrease in the energy density at the cell level. Hence, freestanding electrodes have captured considerable attention due to their enhanced performance, e.g., NiFe₂O₄/C binder-free electrodes [30], metal-oxide/C self-standing electrodes [31], and self-supported Li₄Ti₅O₁₂ nanosheet array electrodes [32]. This is because the free-standing electrode structure can accelerate Li⁺ ion and electron transfer, preserving the flexibility and integrity of the electrode, and simplify the cell packing process, contributing to high electrochemical performance.

To alleviate the drastic volume variation and unstable SEI formation while simultaneously enhancing the electronic conductivity of Si, herein, free-standing N-doped porous C nanofibers sheathed pumpkin-like Si/C composites (Si/C-ZIF-8/CNFs) are fabricated by electrospinning and carbonization methods. With structural advantages, the as-obtained free-standing Si/C-ZIF-8/CNFs electrode demonstrates outstanding electrochemical performance, achieving a high capacity of 945.5 mA h g $^{-1}$ at 0.2 A g $^{-1}$ after 150 cycles when applied as an anode for LIBs. Moreover, a full cell with a Si/C-ZIF-8/CNFs anode displays a capacity of over 63.4 mA h g $^{-1}$ after 100 cycles at 0.2C, with a capacity retention of 60%, suggesting this composite may have great potential for practical application.

2. Experimental

2.1. Preparation of Si/ZIF-8

1.47 g of Zn(NO₃)₂·6H₂O is mixed in 50 mL of methanol to form a homogeneous solution A, then 0.2 g of Si nanoparticles (Shanghai Gexin Nano Technology Co., Ltd., 99.9%) are dispersed into solution A using an ultrasonic method. 1.54 g of 2-methylimidazole (Aladdin, 98%) is dissolved into another 50 mL of methanol as solution B. Solution A is mixed with solution B, stirred vigorously at room temperature for 24 h, and centrifuged and washed with methanol for 3 times. Si/ZIF-8 is obtained after the mixture is dried at 70 °C for 12 h in a vacuum condition.

2.2. Synthesis of Si/C-ZIF-8/CNFs

0.35 g of the as-prepared Si/ZIF-8 is ultrasonically dispersed in *N*, *N*-dimethylformamide, followed by the addition of 0.4 g of poly-

acrylonitrile (PAN, Aladdin, $M_{\rm w}$ = 150,000), and stirred at 60 °C for 1 h. Then, the mixture is naturally cooled to room temperature and stirred for 12 h. Subsequently, a syringe with a 21 gauge needle is filled with the homogeneous mixture. Aluminum foil is used as a collector, and the distance between the needle and collector is 15 cm. The electrospinning process is carried out at a working voltage of 18 kV and flow rate of 1.0 mL h⁻¹. The precursor is preoxidation at 280 °C for 3 h, and the mixture is then kept at 950 °C for 3 h under an N₂ atmosphere to obtain Si/C-ZIF-8/CNFs. For comparison, Si/ZIF-8 is directly carbonized at 950 °C for 3 h in nitrogen to obtain Si/C-ZIF-8.

2.3. Materials characterization

The morphology of the complexes is obtained by a scanning electron microscope (FE-SEM, S-4800, Hitachi, Japan) equipped with an energy-dispersive X-ray spectrometer (EDX) and transmission electron microscope (TEM, H-600, Hitachi, Japan). The crystalline phases of the samples are performed using X-ray diffraction (XRD, Bruker D8 Advance equipped with Cu Kα radiation). Surface analysis of the complexes is taken with an X-ray photoelectron spectroscope (XPS, PHI 5000 VersaProbe). The elemental mapping analysis displays the distribution of the sample. The content of Si of the as-prepared materials is determined by thermogravimetric analysis (TGA, Netzsch SDT 449F3). The surface area and porosity analysis are acquired on an ASAP 2050 analyzer.

2.4. Electrochemical measurements

The Si/C-ZIF-8/CNFs anode is directly cut into circular discs and then dried at 80 °C for 12 h under vacuum, while the Si/C-ZIF-8 anode is obtained by coating with a uniform slurry of the Si/C-ZIF-8, sodium alginate binder, and acetylene black conductive additive in a weight ratio of 70:15:15. The anode is dispersed in deionized water on copper, dried at 80 °C under vacuum for 12 h, and then punched into circular discs; the mass loading of active materials is \sim 0.8–1.2 mg cm $^{-2}$. The measured specific capacity of the Si/C-ZIF-8/CNFs anode is based on the whole mass of Si/C-ZIF-8/CNFs. The cell is assembled in an argon-filled glove box with Si/C-ZIF-8/CNFs (Si/C-ZIF-8 or Si electrode), Celgard 2400, Li foil, and LiPF₆ (1 M) in dimethyl carbonate (DMC) and ethylene carbonate (EC) in a volume ratio of 1:1, including 5 wt% vinylene carbonate (VC) as the working electrode, separator membrane, counter electrode, and electrolyte, respectively. The galvanostatic charge and discharge testing are carried out by a Land battery test system (Wuhan, China), which is performed at 0.01-1.5 V (versus Li/Li⁺). The cyclic voltammetry (CV, CHI660D Chenhua, China) is set to be 0.1 mV s⁻¹ at a voltage interval of 0.01–1.5 V (versus Li/Li⁺). The electrochemical impedance spectra (EIS) are collected from a ZAHNER-elektrik electrochemical workstation and measured with a 10 mV amplitude in the frequency range of 0.1 Hz-100 kHz. To set up a full cell, the Si/C-ZIF-8/CNFs anode is combined with a LiNi_{1/3}Co_{1/3}Mn_{1/3}O₂ (NCM) cathode. Typically, the cathode is fabricated by commercial NCM, acetylene black (AB), and polyvinylidene difluoride (PVDF) (at a weight ratio of 8:1:1) on aluminum foil, and the same separator membrane and electrolyte are used. The galvanostatic charge and discharge testing as well as cycle performance of NCM half cells and NCM /Si/C-ZIF-8/CNFs full cells are carried out by a Land battery test system, which are performed at voltage range of 2.5-4.5 V and 2.8-4.3 V, respectively.

3. Results and discussion

The schematic for the preparation of Si/C-ZIF-8/CNFs is illustrated in Fig. 1(a). The Si/ZIF-8 is first fabricated through a solvent

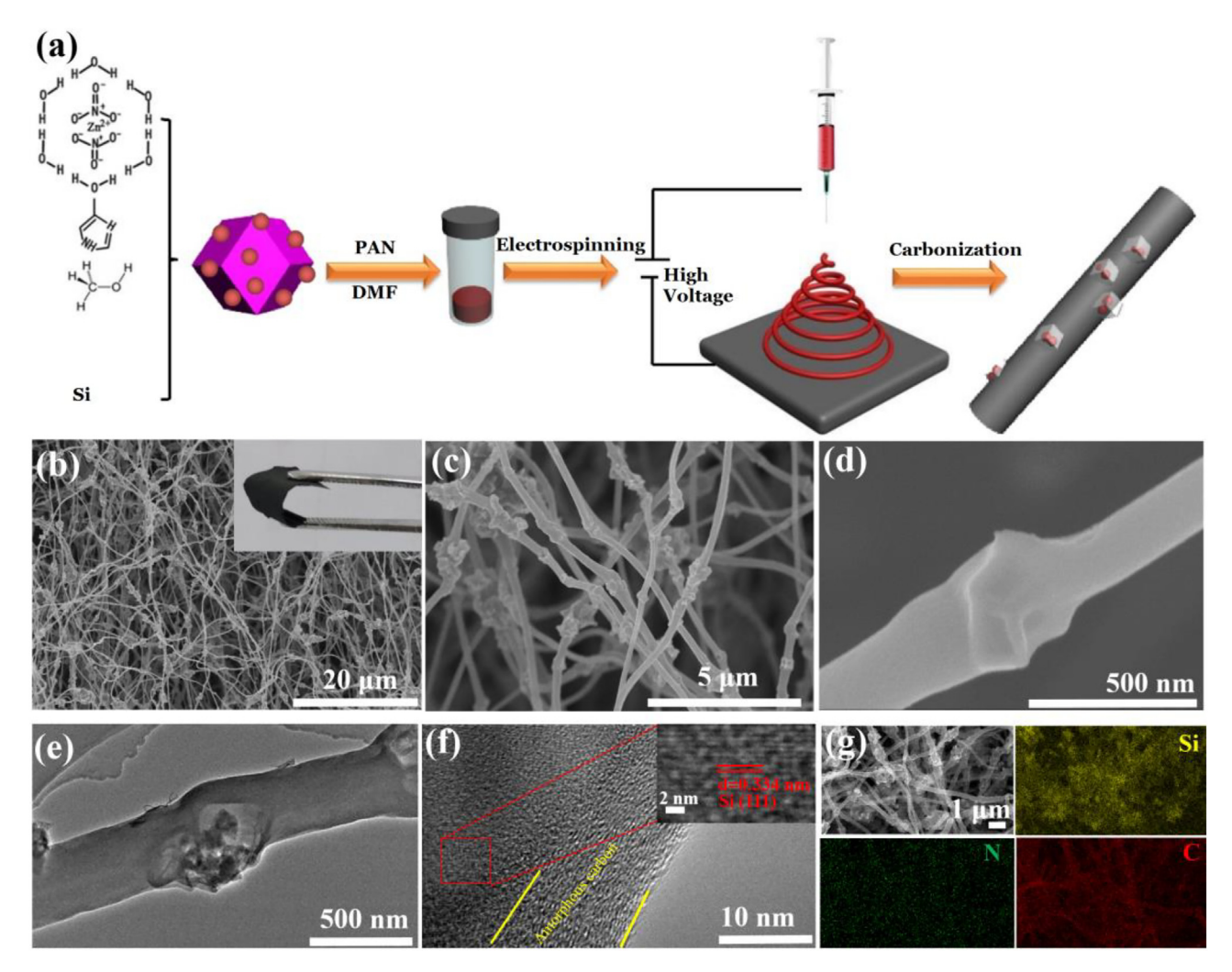


Fig. 1. (a) Schematic for the preparation of Si/C-ZIF-8/CNFs. (b-d) FESEM images of Si/C-ZIF-8/CNFs (inset in (b) is its corresponding photograph). (e,f) TEM images of Si/C-ZIF-8/CNFs (inset in (f) is its HRTEM image taken from the rectangular area marked in (f)). (g) FESEM image and elemental mapping images of Si/C-ZIF-8/CNFs.

method, then Si/ZIF-8 is mixed with PAN in DMF, and the mixture forms nanofibers by an electrospinning method. After heat treatment at 950 °C in the $\rm N_2$ atmosphere, ZIF-8 and PAN are decomposed and transformed into an N-doped porous carbon layer, and the self-supporting Si/C-ZIF-8/CNFs membrane is obtained. During the carbonation process, most of the ZnO in ZIF-8 is reduced to Zn nanoparticles, and are removed owing to their low boiling point (907 °C) [33]. Therefore, they can leave many pores in the carbon nanofibers. Benefitting from the porous structure, Si nanoparticles can enter the void derived from ZIF-8 pyrolysis. Eventually, Si/C-ZIF-8/CNFs form a pumpkin-like structure; however, the specific formation mechanism still needs to be further studied. On the contrary, Si/C-ZIF-8 is carbonized directly from Si/ZIF-8 without electrospinning, which does not possess a pumpkin-like structure.

The morphologies of naked Si are characterized by SEM, as shown in Fig. S1(a,b). The naked Si exhibits a spherical morphology with a diameter ranging from 30 – 50 nm. According to the FESEM image in Fig. S1(c,d), the as-prepared Si/ZIF-8 is composed of many Si nanoparticles and ZIF-8; the Si nanoparticles are accumulated on the surface of the ZIF-8. After the electrospinning process, the asprepared Si/ZIF-8/PAN exhibits a nanofiber structure (Fig. S2). Through the carbonization process in N₂, the resultant Si/C-ZIF-8/CNFs retain the same fiber-like shape (Fig. 1b). The high-magnification FESEM image shows that the average size of the Si/

C-ZIF-8/CNFs is approximately 500 nm, and the Si nanoparticles are completely wrapped in fibers (Fig. 1c). In addition, some regular carbon polyhedra in Si/C-ZIF-8/CNFs are revealed, which are similar to the pumpkin shape (Fig. 1d). Meanwhile, benefitting from the conductive network formed by C nanofibers, Si/C-ZIF-8/ CNFs display good flexibility (inset in Fig. 1b). The FESEM image of Si/C-ZIF-8 is given in Fig. S3, which presents a nanoparticle morphology. The cross-section image of the Si/C-ZIF-8/CNFs membrane clearly shows that its thickness is approximately 200 µm (Fig. S4). Moreover, it can be obviously found that one-dimensional C nanofibers are piled layer by layer, and the subsequent 3D porous structure is obtained, which can facilitate Li⁺ ion and electron transport [34]. The TEM image (Fig. 1e) further indicates that the Si nanoparticles are dispersed in the C polyhedra. The pumpkin-like structure is carbonized to form a pumpkin shell at high temperature by ZIF-8, and the Si nanoparticles exist in the pumpkin together constituting the "pumpkin seeds". Additionally, the large space derived from ZIF-8 can be observed between the Si nanoparticle core and the N-doped porous C shell, which can alleviate the volume expansion of Si during the charge-discharge process [35]. The high-resolution TEM (HRTEM) image shown in the inset of Fig. 1 (f) displays lattice fringes with a d-spacing of 0.334 nm, which is consistent with the (111) plane of Si. No obvious lattice fringes of C are found, which indicates that the C is amorphous (Fig. 1f). The FESEM image and mapping image of Si (yellow), C (red), and

N (green) of Si/C-ZIF-8/CNFs shown in Fig. 1(g) confirms the uniform distribution of elements in the sample.

The purity and crystalline phase of Si/C-ZIF-8/CNFs, Si/C-ZIF-8, and pure Si are investigated by XRD (Fig. 2a). Both Si/C-ZIF-8/CNFs and Si/C-ZIF-8 samples exhibit clear peaks of the (111), (220), (311), (400), and (331) planes, which match well with the Si (JCPDS no. 27–1402), indicating that the addition of ZIF-8 and PAN does not lead to the change in the crystal structure of Si. Moreover, no Zn peak is found in the XRD pattern of either sample, meaning that Zn has been removed during the carbonization process [36].

The surface states and chemical composition of Si/C-ZIF-8/CNFs are performed by XPS. From the XPS survey spectra (Fig. S5), the existence of Si, C, N, and O elements on the surface of Si/C-ZIF-8/ CNFs can be observed. As the Si 2p XPS spectra shows in Fig. 2 (b), two peaks centered at 99.3 and 99.8 eV belong to the Si-Si bond [37], while the peaks with the binding energy of 102.5 and 103.2 eV can be ascribed to SiO_x [38], which show that there are silica or Si oxides in the sample. However, the XRD peaks of silica or Si oxides are not found in Fig. 2(a), demonstrating that the quantity of silica or Si oxides is low. The N 1s XPS spectra (Fig. 2c) consists of three peaks at approximately 404.8, 398.6, and 400.9 eV, which correspond to graphitic-N, pyridinic-N, and pyrrolic-N, respectively [39]. The presence of pyridinic-N and pyrrolic-N can accelerate the transfer of electrons and provide abundant electrochemical active sites for Li⁺ ions [8], while the graphitic N is a benefit to improve the electrical conductivity of the C layer [40]. In the C 1s XPS spectra (Fig. 2d), the peaks at 284.7 and 289.3 eV are fitted with C-C and C = O bonds [41], respectively. Peaks at 286.4 and 291.1 eV are assigned to C-O-H and C-O-C bonds [42], respectively. The peak at 532.3 eV corresponds to the O 1s XPS spectrum, which may arise from the oxidation of Si during the preparation process. (Fig. 2e) [43].

N₂ adsorption–desorption isotherms are performed to study the surface area and pore structure of Si/C-ZIF-8/CNFs and Si/C-ZIF-8 samples. In Fig. 2(f), a type IV curve with a hysteresis loop at P/P_0 between 0.4-1.0 is observed by the N₂ adsorption-desorption isotherm of Si/C-ZIF-8/CNFs. The result suggests that Si/C-ZIF-8/CNFs contain mesoporous structures [44,45]. The specific surface area and pore size of Si/C-ZIF-8/CNFs are approximately 110.476 m² g^{-1} and ~ 3.8 nm, respectively. Compared to the specific surface area of Si/C-ZIF-8 (64.198 m² g⁻¹), the increase in specific surface area may be ascribed to the synergistic effect between ZIF-8 and PAN in the carbonation process, which results in the formation of pores in the PAN-based C. The N₂ adsorption-desorption isotherms of Si/ C-ZIF-8 do not possess a type H1 hysteresis loop, reflecting the Si/ C-ZIF-8 accounts of several mesoporous structures. During the carbonation process. Si/C-ZIF-8 is carbonized directly from Si/ZIF-8 because Si/C-ZIF-8 is not coated by C derived from PAN, and thus does not form pores. Furthermore, Si/C-ZIF-8 are not connected due to the absence of PAN, which might retard the rate of Li⁺ ion and electron transfer. Obviously, the highly specific surface area and mesoporous structure of Si/C-ZIF-8/CNFs not only speed up the transfer of electrons and Li⁺ ions, but also enrich more Li storage sites [46]. According to the TGA in Fig. S6, Si/C-ZIF-8/CNFs consist of 54.5% Si. It also can be observed that the Si proportion of Si/C-ZIF-8/ CNFs is lower than that of Si/C-ZIF-8 (90.7%), which might be attributed to adding PAN into Si/C-ZIF-8/CNFs.

The Li storage behaviors are examined by CV measurements. CV curves of the first five cycles of the Si/C-ZIF-8/CNFs electrode at 0.1 mV s $^{-1}$ in a voltage range of 0.01–1.5 V are presented in Fig. 3(a). A broad peak at 0.8 V is observed in the first cathodic cycle, and then vanishes in the following cycles, resulting from the formation of SEI film and the irreversible reaction of Li $^{+}$ ions on the surface [47]. A cathodic peak at 0.2 V appears in the second cycle of Si/C-ZIF-8/CNFs, corresponding to the reaction of Si with

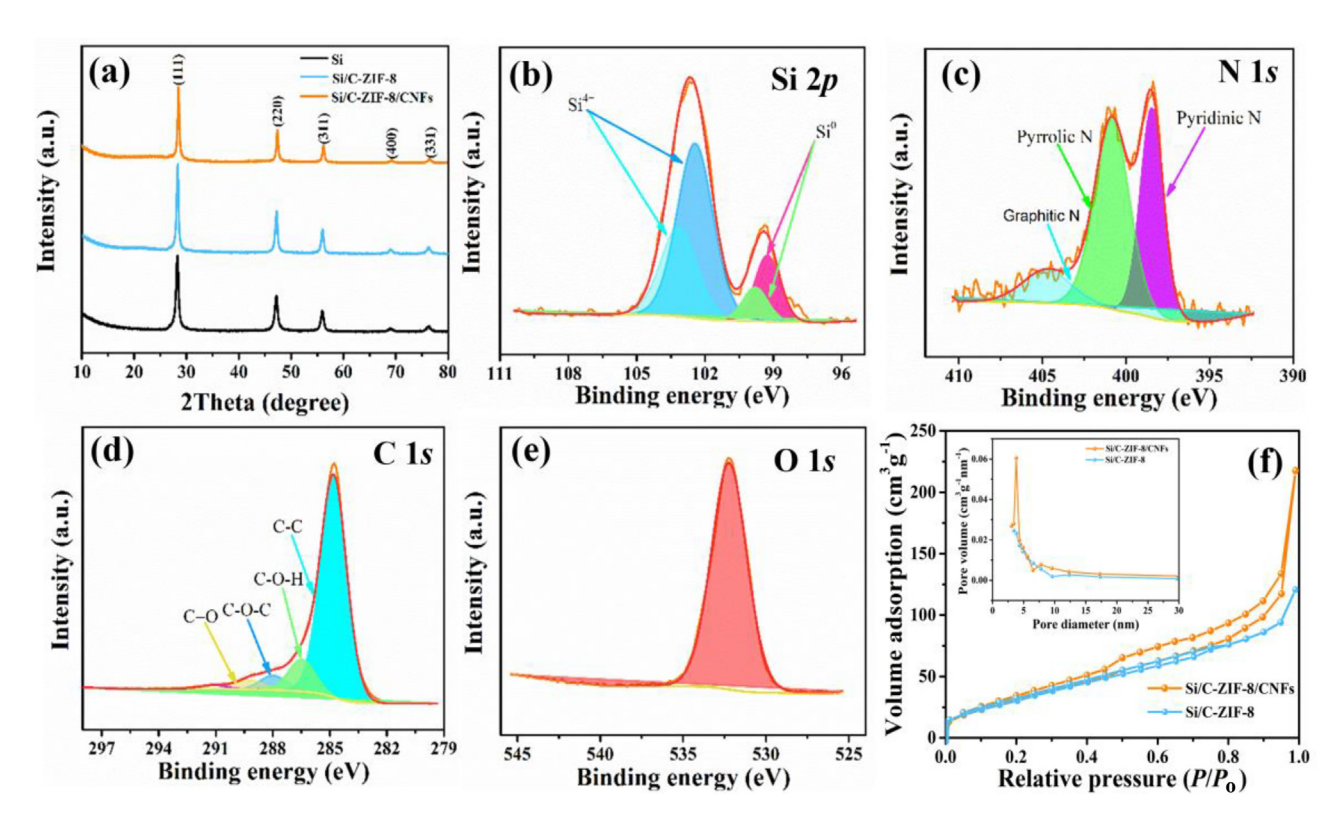


Fig. 2. Structural characterization of the samples: (a) XRD patterns, high-resolution (b) Si 2p, (c) N 1s, (d) C 1s, and (e) O 1s XPS spectra of Si/C-ZIF-8/CNFs. (f) Nitrogen adsorption–desorption isotherm with a pore-size distribution (inset) curve of the Si/C-ZIF-8/CNFs and Si/C-ZIF-8.

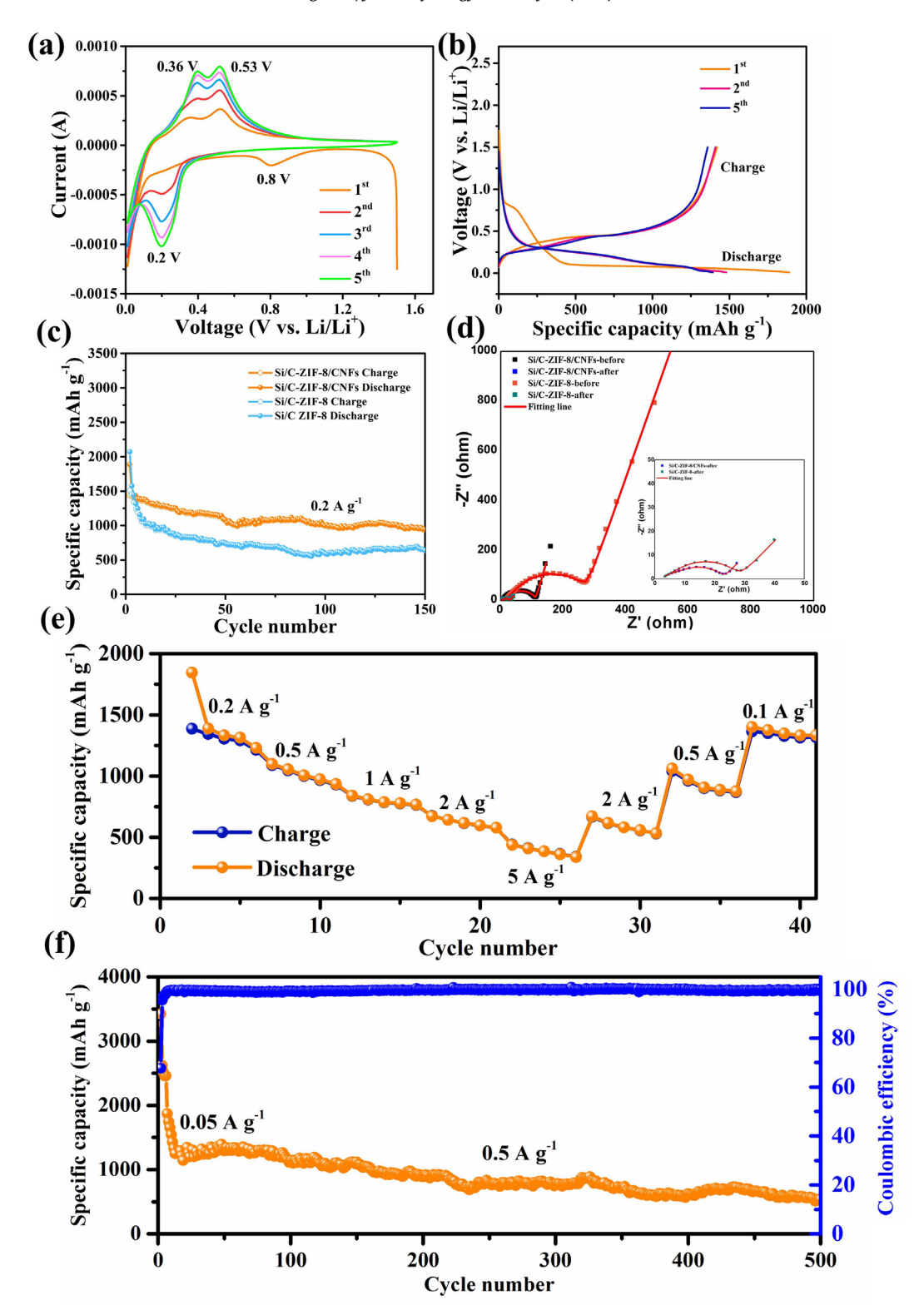


Fig. 3. Electrochemical performance in a half cell: (a) CV curves of the first five cycles of the Si/C-ZIF-8/CNFs electrode at 0.1 mV s⁻¹ in a voltage range of 0.01-1.5 V, (b) galvanostatic charge–discharge curves of Si/C-ZIF-8/CNFs for the 1st, 2nd, and 5th cycles at 0.2 A g⁻¹, (c) cycle performance of Si/C-ZIF-8/CNFs and Si/C-ZIF-8 electrodes at 0.2 A g⁻¹ for 150 cycles, (d) EIS spectra of Si/C-ZIF-8/CNFs and Si/C-ZIF-8 electrodes before and after 150 cycles (inset in Fig. 3(d) is the enlarged view of Si/C-ZIF-8/CNFs and Si/C-ZIF-8 electrodes after cycling). (e) rate performance of Si/C-ZIF-8/CNFs electrode and (f) long-term cycling performance of Si/C-ZIF-8/CNFs electrode at a current density of 0.5 A g⁻¹ after cycling with the first five cycles at 0.05 A g⁻¹.

Li⁺ [48]. Apart from that, there are two peaks located at ~ 0.36 V and ~ 0.6 V in the anodic cycle, which are derived from the delithiation of Li_xSi [49]. Although silica or Si oxides are found in XPS, it can be demonstrated from the CV that only Si is involved in the

electrochemical reactions. The redox peaks are similar to the previous report [50].

The galvanostatic charge–discharge behaviors of both samples at 0.2 A g^{-1} in a voltage range of 0.01-1.5 V after different cycles

are shown in Fig. 3(b) and Fig. S7. Si/C-ZIF-8 displays a first cycle discharge capacity of 2076.5 mA h g⁻¹ at 0.2 A g⁻¹ with a coulombic efficiency of 73% (Fig. S7). In comparison, the first cycle discharge capacity of Si/C-ZIF-8/CNFs is 1888.8 mA h g⁻¹ with a coulombic efficiency of nearly 76%. The relatively high initial coulombic efficiency can be related to the introduced N-doped porous C shell, which contributes to form the stable SEI [51]. Although the initial coulombic efficiency of this work is not high, it is improved compared to the value reported in previous literature, as shown in Table S1. A long, flat plateau at 0.1 V is observed in the first discharge curve of Si/C-ZIF-8/CNFs, corresponding to the typical electrochemical behavior of the Li-Si alloy process [48]. Another obvious plateau is exhibited at 0.8 V and vanishes in the subsequent cycle, which belongs to the SEI formation [52]. The initial capacity loss is considered as the result of the formation of the SEI layer and the irreversible trapping of Li⁺ in Li_vSi [53], which can be compensated by pre-lithiation through either chemical or electrochemical methods or by using stabilized Li metal powder [5]. From the charge/discharge curves, it can be seen that Si/C-ZIF-8/ CNFs have better overlap than that of Si/C-ZIF-8 in the 1st, 2nd, and 5th cycles, indicating the good cycle stability of Si/C-ZIF-8/ CNFs.

Fig. 3(c) shows the cycle performance of both samples at 0.2 A g $^{-1}$. Obviously, Si/C-ZIF-8/CNFs exhibit a significantly improved cycling performance with a high discharge capacity of 945.5 mA h g $^{-1}$ after 150 cycles. The corresponding capacity retention of Si/C-ZIF-8/CNFs is maintained at 64% from the 2nd to 150th cycles. The capacity attenuation of Si is probably due to some HF corrosion of Si caused by LiPF $_6$ decomposition in the electrolyte [54]. The formation of SEI on the electrode surface is due to the electrochemical reduction of organic salt and solvent, and its mor-

phology and composition mainly depend on the composition of the electrolyte. It not only affects the kinetics of Li⁺ ion charge/discharge, but also the surface stability during the long cycle [55–58]. In contrast, Si/C-ZIF-8 exhibits a discharge capacity of 646.7 mA h g⁻¹ after 150 cycles. The corresponding capacity retention of Si/C-ZIF-8 is maintained at 41% from the 2nd to 150th cycles. The reason for the higher capacity retention of the Si/C-ZIF-8/CNFs electrode as compared to that of the Si/C-ZIF-8 electrode could be ascribed to the void in the pumpkin-like structure, which can buffer the volume expansion of Si during the cycling process.

To realize the conductivity and ion diffusion, the electrochemical impedance spectroscopy (EIS) of Si/C-ZIF-8/CNFs and Si/C-ZIF-8 electrodes before cycling and after 150 cycles are demonstrated and fitted in Fig. 3(d). The EIS shows that both samples consist of one semicircle and one line. The semicircle in the high and middle-frequency region is associated with the interfacial charge transfer resistance (R_{ct}) , which affects the electrochemical kinetics [58]. The low-frequency line is due to Warburg impedance (W_0) , which is connected with Li^+ ion diffusion [59]. The R_{ct} of the Si/ C-ZIF-8/CNFs electrode before (75.51 Ω) and after (16.62 Ω) cycling is lower than that of the Si/C-ZIF-8 electrode before (198.1 Ω) and after (22.07 Ω) cycling, reflecting that Si/C-ZIF-8/ CNFs possess enhanced electrical conductivity. This is because the N-doped porous carbon derived from ZIF-8 and PAN provides more Li⁺ ion storage sites and a 3D conductive network of Si/C-ZIF-8/CNFs provides faster electron and Li⁺ ion transfer [60].

Fig. 3(e) displays the rate performance of Si/C-ZIF-8/CNFs. The discharge capacity of Si/C-ZIF-8/CNFs is approximately 1845.4, 1097.2, 840.3, 672.5, and 437.4 mA h g $^{-1}$ at 0.2, 0.5, 1, 2, and 5 A g $^{-1}$, respectively. More importantly, when the current rate returns

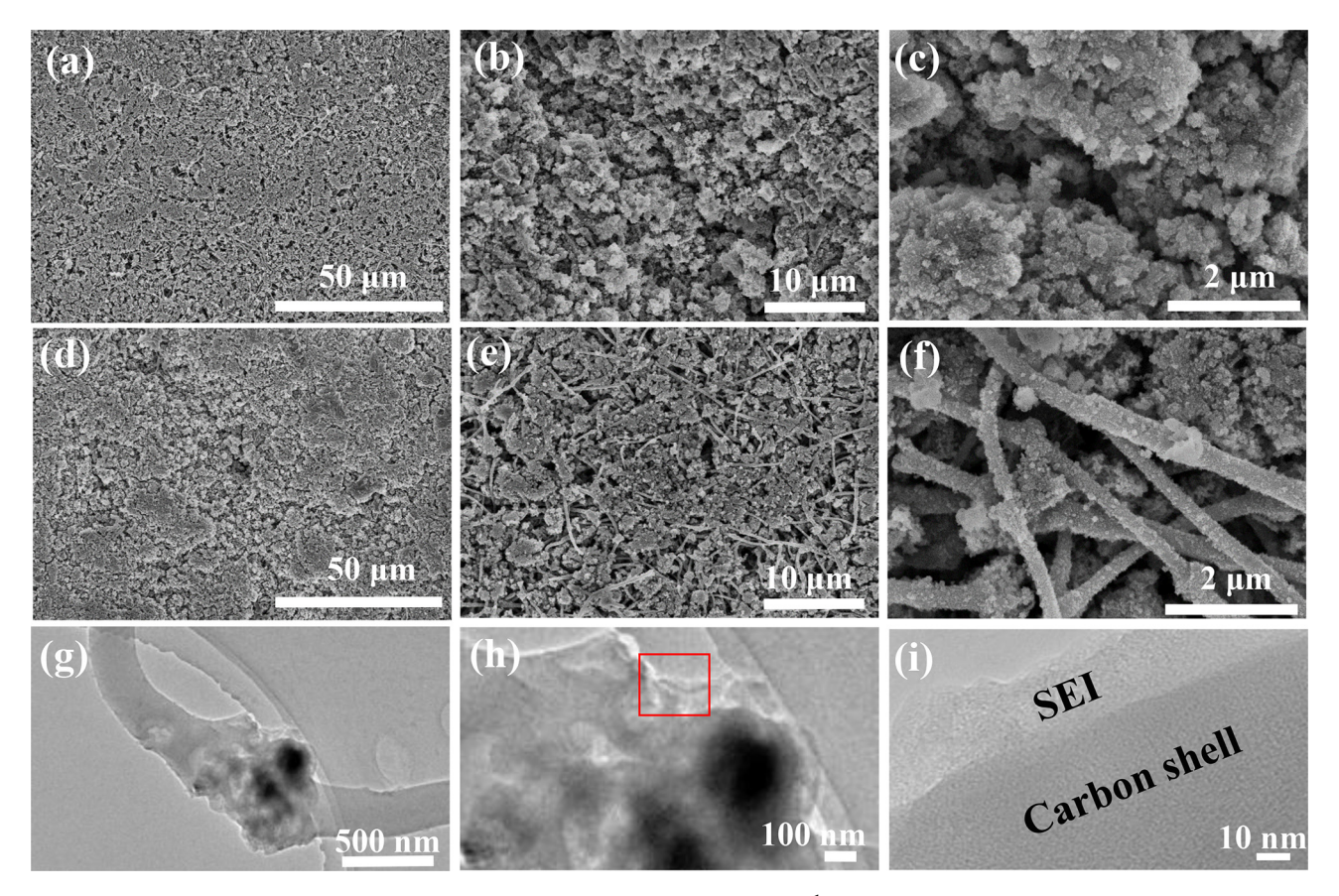


Fig. 4. (a-c) SEM images of Si/C-ZIF-8 and (d-f) Si/C-ZIF-8/CNFs electrodes after 150 cycles at 0.2 A g⁻¹ with different magnifications. (g-i) TEM images of Si/C-ZIF-8/CNFs electrode after 150 cycles at 0.2 A g⁻¹ with different magnifications, Fig. 4(i) is taken from the rectangular area marked in Fig. 4(h).

to 0.1 A g^{-1} , the sample displays a discharge capacity of $1334.4 \text{ mA h g}^{-1}$, verifying that it possesses good rate performance.

To further validate the cycling performance of Si/C-ZIF-8/CNFs at high current density, the Si/C-ZIF-8/CNFs electrode is detected at 0.5 A $\rm g^{-1}$ for over 500 cycles, and the corresponding result is presented in Fig. 3(f). The Si/C-ZIF-8/CNFs anode displays a capacity of approximately 538.6 mA h $\rm g^{-1}$ after 500 cycles and the initial coulombic efficiency is 68%. The ameliorated electrochemical behavior can be ascribed to a distinctive pumpkin-like structure, which can partly reduce the volume variation and release the mechanical stress. In addition, the result of the electrochemical performance of the bare Si nanoparticles electrode is displayed in Fig. S8. Compared with the bare Si nanoparticles electrode, the Si/C-ZIF-8/CNFs and Si/C-ZIF-8 electrodes demonstrate significantly enhanced electrochemical performance.

Fig. 4 displays the SEM images of the Si/C-ZIF-8/CNFs and Si/C-ZIF-8 electrodes after 150 cycles at 0.2 A g⁻¹. As shown in Fig. 4(d-f), the Si/C-ZIF-8/CNFs electrode retains a nanofiber structure without obvious fracture. Nevertheless, the Si/C-ZIF-8 electrode (Fig. 4a-c) displays many cracks, which may cause loose contact between the Cu foil and the active material, further resulting in fast capacity fading. To confirm that the material can suppress the volume expansion of Si and favor the formation of a stable SEI, the Si/C-ZIF-8/CNFs electrode material is detected by TEM after 150 cycles. From Fig. 4(g-h), it can be observed that Si nanoparticles expand and fill the void after cycling, but the structure remains intact and does not break, preserving the integrity of the electrode structure. The surface of the C shell of Si/C-ZIF-8/

CNFs has a uniform SEI layer (Fig. 4i). It clearly shows that the materials can effectively buffer the volume expansion and prevent the unstable SEI layer formation.

Considering the practicality of Si/C-ZIF-8/CNFs in commercial LIBs, full cells are assembled with Si/C-ZIF-8/CNFs as the anode and NCM as the cathode. The initial charge-discharge curves with cycling data of NCM half cells and NCM /Si/C-ZIF-8/CNFs full cells are set at different voltage windows, which are shown in Fig. (5a and c). The specific capacity is calculated based on the total mass of the cathode, and its mass loading is 23.25 mg cm⁻². The initial charge-discharge profile of NCM with cycling data is depicted in Fig. 5(a,b); the charge/discharge capacity is 226.3/194.7 mA h g⁻¹ at 0.2 C in the first cycle (1 C = 200 mA h g^{-1}). The capacity remains at 149.9 mA h g^{-1} after 100 cycles between 2.5 and 4.5 V. Fig. 5(c,d) show the initial charge-discharge curves of the full cell together with cycle data at a current density of 0.2 C between 2.8 and 4.3 V. A reversible capacity of 106.1 mA h g^{-1} can be obtained in the full cell and the initial coulombic efficiency is 57%. Additionally, the full cell can deliver a reversible capacity of 63.4 mA h g^{-1} after 100 cycles with a capacity retention of 60%.

Overall, the electrochemical performance of Si/C-ZIF-8/CNFs can be enhanced. The properties of Si/C-ZIF-8/CNFs are compared with those of other Si/C composites in previous literature, and the results are listed in Table S2. The electrochemical performance of Si/C-ZIF-8/CNFs are better than that of the previously reported results (Table S2). The enhanced electrochemical performance can be understood for the following reasons. Firstly, the void in the pumpkin-like structure helps buffer the volume expansion of

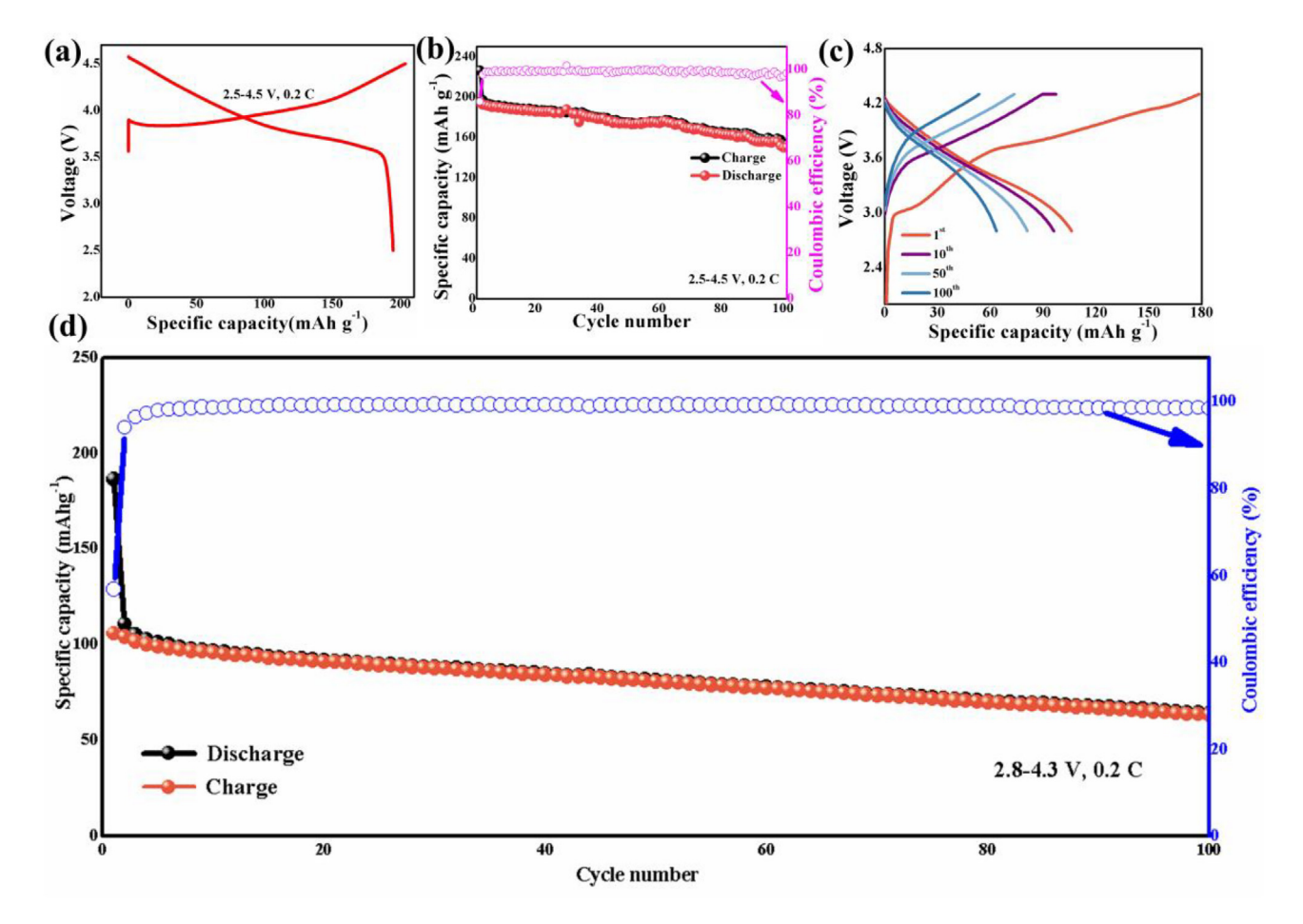


Fig. 5. (a) Charge-discharge profile and (b) cycling performance of the NCM half cells; (c) charge-discharge profile and (d) cycling performance of the NCM/Si/C-ZIF-8/CNFs full cells.

Si nanoparticles, thereby enhancing its cycle performance. Secondly, the Si nanoparticles are distributed in an N-doped porous C, which prevents direct contact between the electrolyte and Si nanoparticles, and favors the formation of stable SEI. Thirdly, N-doped porous C is a good conductor of electrons and provides abundant electrochemical active sites, which contributes to improving the electrochemical conductivity [61]. Finally, the free-standing structure can mitigate the resistance of electron and Li⁺ ion transfer, further improving the rate capability.

4. Conclusions

In summary, free-standing N-doped porous C nanofibers sheathed pumpkin-like Si/C composites are successfully prepared, exhibiting high specific capacity and superior cycling and rate performance when applied as an anode for LIBs. Specifically, the composite displays an initial coulombic efficiency of 76%, and a high reversible capacity of 945.5 mA h g $^{-1}$ at 0.2 A g $^{-1}$ with a capacity retention of 64% after 150 cycles. It also shows good rate capability with a reversible capacity of 538.6 mA h g $^{-1}$ at 0.5 A g $^{-1}$ over 500 cycles. Interestingly, the full cell using the free-standing Si/C-ZIF-8/CNFs anode and NCM cathode demonstrates a reversible capacity of \sim 63.4 mA h g $^{-1}$ after 100 cycles. Our findings in this work could provide a new way to fabricate high-performance Si-based anodes for LIBs.

Declaration of Competing Interest

The authors declare that they have no known competing financial interests or personal relationships that could have appeared to influence the work reported in this paper.

Acknowledgments

This work is financially supported by the National Natural Science Foundation of China (Grant Nos. 21965034, 21703185, U1903217, 51901013, and 21666037), the Xinjiang Autonomous Region Major Projects (2017A02004), the Leading Project Foundation of Science Department of Fujian Province (Grant No. 2018H0034), the Resource Sharing Platform Construction Project of Xinjiang Province (PT1909), the Nature Science Foundation of Xinjiang Province (2017D01C074), the Opening Project of National Joint Engineering Research Center for Abrasion Control and Molding of Metal Materials, Henan University of Science and Technology (No. HKDNM201906), and the Young Scholar Science Foundation of Xinjiang Educational Institutions (XJEDU2016S030).

Appendix A. Supplementary data

Supplementary data to this article can be found online at https://doi.org/10.1016/j.jechem.2020.06.022.

References

- [1] J.B. Goodenough, K.S. Park, J Am Chem Soc 135 (2013) 1167-1176.
- [2] B. Dunn, H. Kamath, J.M. Tarascon, Science 334 (2011) 928–935.
- [3] Y. Zhang, D. Jia, Y. Tang, Y. Huang, W. Pang, Small 14 (2018) 1704354-1704361. (2018).
- [4] W. An, B. Gao, S. Mei, B. Xiang, J. Fu, L. Wang, Q. Zhang, P.K. Chu, K. Huo, Nat. Commun. 10 (2019) 1447.
- [5] Q. Zhang, H. Chen, L. Luo, B. Zhao, H. Luo, X. Han, J. Wang, C. Wang, Y. Yang, T. Zhu, M. Liu, Energy Environ. Sci. 11 (2018) 669–681.
- [6] X. Wang, W. Jia, L. Wang, Y. Huang, Y. Guó, Y. Sun, D. Jia, W. Pang, Z. Guo, X. Tang, J. Mater. Chem. A 4 (2016) 13907–13915.
- [7] X. Zhang, X. Cheng, Q. Zhang, J. Energy Chem. 25 (2016) 967–984.
- [8] J. Liu, J. Liang, C. Wang, J. Ma, J. Energy Chem. 33 (2019) 160–166.

- [9] Z. Zheng, P. Li, J. Huang, H. Liu, Y. Zao, Z. Hu, L. Zhang, H. Chen, M.-S. Wang, D.-L. Peng, Q. Zhang, J. Energy Chem. 41 (2020) 126–134.
- [10] Q. Li, D. Chen, H. Tan, X. Zhang, X. Rui, Y. Yu, J. Energy Chem. 40 (2020) 15–21.
- [11] M. Yoshio, H. Wang, K. Fukuda, T. Umeno, T. Abe, Z. Ogumi, J. Mater. Chem. A 14 (2004) 1754–1758.
- [12] M. Xia, B. Chen, F. Gu, L. Zu, M. Xu, Y. Feng, Z. Wang, H. Zhang, C. Zhang, J. Yang, ACS Nano 14 (2020) 5111–5120.
- [13] X. Han, Z. Zhang, S. Chen, Y. Yang, J. Power Sources 463 (2020) 228245–228253.
- [14] S.D. Beattie, D. Larcher, M. Morcrette, B. Simon, J.M. Tarascon, J. Electrochem. Soc 155 (2008) A158–A163.
- [15] A. Mukanova, A. Jetybayeva, S.-T. Myung, S.-S. Kim, Z. Bakenov, Mater. Today, Energy 9 (2018) 49–66.
- [16] N. Liu, X. Mamat, R. Jiang, W. Tong, Y. Huang, D. Jia, Y. Li, L. Wang, T. Wågberg, G. Hu, Chem. Eng. J. 343 (2018) 78–85.
- [17] W. Wang, P.N. Kumta, ACS Nano 4 (2010) 2233-2241.
- [18] Z. Zheng, H.H. Wu, H. Chen, Y. Cheng, Q. Zhang, Q. Xie, L. Wang, K. Zhang, M.S. Wang, D.L. Peng, X.C. Zeng, Nanoscale 10 (2018) 22203–22214.
- [19] N.S. Hieu, J.C. Lim, J.K. Lee, Microelectronic Eng. 89 (2012) 138-140.
- [20] A.M. Chockla, J.T. Harris, V.A. Akhavan, T.D. Bogart, V.C. Holmberg, C. Steinhagen, C.B. Mullins, K.J. Stevenson, B.A. Korgel, J. Am. Chem. Soc. 133 (2011) 20914–20921.
- [21] H. Wu, G. Chan, J.W. Choi, I. Ryu, Y. Yao, M.T. McDowell, S.W. Lee, A. Jackson, Y. Yang, L. Hu, Nat. Nanotech. 7 (2012) 310–315.
- [22] Y. An, H. Fei, G. Zeng, L. Ci, S. Xiong, J. Feng, Y. Qian, Green, ACS Nano 12 (2018) 4993–5002.
- [23] Z. Lu, J. Zhu, D. Sim, W. Zhou, W. Shi, H.H. Hng, Q. Yan, Chem. Mater. 23 (2011) 5293–5295.
- [24] A. Gohier, B. Laik, K.H. Kim, J.L. Maurice, J.P. Pereira-Ramos, C.S. Cojocaru, P.V. Tran, Adv. Mater. 24 (2012) 2592–2597.
- [25] B. Chen, L. Zu, Y. Liu, R. Meng, Y. Feng, C. Peng, F. Zhu, T. Hao, J. Ru, Y. Wang, J. Yang, Angew Chem Int Ed Engl 59 (2020) 3137–3142.
- [26] Y. Zheng, S. Zheng, H. Xue, H. Pang, Adv. Funct. Mater. 28 (2018) 1804950– 1804978.
- [27] N. Liu, J. Liu, D. Jia, Y. Huang, J. Luo, X. Mamat, Y. Yu, Y. Dong, G. Hu, Energy Storage Mater. 18 (2019) 165–173.
- [28] Q. Bai, F.-C. Shen, S.-L. Li, J. Liu, L.-Z. Dong, Z.-M. Wang, Y.-Q. Lan, Small Methods 2 (2018) 1800049–1800057.
- [29] K.S. Park, Z. Ni, Á.P. Côté, J.Y. Choi, R. Huang, F.J. Uribe-Romo, H.K. Chae, M. O'Keeffe, O.M. Yaghi, Proc. Natl. Acad. Sci. USA 103 (2006) 10186–10191.
- [30] X. Zhang, C. Wang, Y.-N. Chen, X.-G. Wang, Z. Xie, Z. Zhou, J. Power Sources 377 (2018) 136–141.
- [31] S.H. Choi, J. Lee, Y.C. Kang, ACS Nano 9 (2015) 10173–10185.
- [32] Q. Xia, N. Jabeen, S.V. Savilov, S.M. Aldoshin, H. Xia, J. Mater. Chem. A 4 (2016) 17543–17551.
- [33] Y. Mao, H. Duan, B. Xu, L. Zhang, Y. Hu, C. Zhao, Z. Wang, L. Chen, Y. Yang, Energy Environ. Sci. 5 (2012) 7950–7955.
- [34] Y. Bai, M. Wang, G. Wang, Y. Ma, Y. Huang, J. Zheng, Nanomaterials (Basel) 9 (2019) 650–666.
- [35] T. Yoon, T. Bok, C. Kim, Y. Na, S. Park, K.S. Kim, ACS Nano 11 (2017) 4808–4815.
- [36] M.J. Wang, Z.X. Mao, L. Liu, L. Peng, N. Yang, J. Deng, W. Ding, J. Li, Z. Wei, Small 14 (2018) 1804183–1804190.
- [37] L. Hu, B. Luo, C. Wu, P. Hu, L. Wang, H. Zhang, J. Energy Chem 32 (2019) 124–130
- [38] M. Gauthier, D. Mazouzi, D. Reyter, B. Lestriez, P. Moreau, D. Guyomard, L. Roué, Energy Environ. Sci. 6 (2013) 2145–2156.
- [39] D. Bhattacharjya, H.-Y. Park, M.-S. Kim, H.-S. Choi, S.N. Inamdar, J.-S. Yu, Langmuir 30 (2014) 318–324.
- [40] W.-M. Chen, L. Qie, Y. Shen, Y.-M. Sun, L.-X. Yuan, X.-L. Hu, W.-X. Zhang, Y.-H. Huang, Nano Energy 2 (2013) 412–418.
- [41] X. Zhang, Z. Sui, B. Xu, S. Yue, B. Liu, J. Mater. Chem. A 21 (2011) 6494–6497.
- [42] G. Zhou, L.-C. Yin, D.-W. Wang, L. Li, S. Pei, I.R. Gentle, F. Li, H.-M. Cheng, ACS Nano 7 (2013) 5367–5375.
- [43] L. Shi, W. Wang, A. Wang, K. Yuan, Y. Yang, J. Mater. Chem. A 2 (2014) 20213–20220.
- [44] J.-G. Wang, H. Liu, H. Sun, W. Hua, H. Wang, X. Liu, B. Wei, Carbon 127 (2018) 85–92.
- [45] Y. Cai, Y. Huang, W. Jia, X. Wang, Y. Guo, D. Jia, Z. Sun, W. Pang, Z. Guo, J. Mater. Chem. A 4 (2016) 9949–9957.
- [46] X. Zhao, W. Jia, X. Wu, Y. Lv, J. Qiu, J. Guo, X. Wang, D. Jia, J. Yan, D. Wu, Carbon 156 (2020) 445–452.
- [47] X. Zhou, Y.-X. Yin, L.-J. Wan, Y.-G. Guo, Chem. Commun. 48 (2012) 2198–2200.
- [48] Y. Xu, Y. Zhu, F. Han, C. Luo, C. Wang, Adv. Energy Mater. 5 (2015) 1400753–1400760.
- [49] H.-Y. Lin, C.-H. Li, D.-Y. Wang, C.-C. Chen, Nanoscale 8 (2016) 1280–1287.
- [50] Z. Luo, Q. Xiao, G. Lei, Z. Li, C. Tang, Carbon 98 (2016) 373–380.
- [51] Y. Chen, Y. Hu, Z. Shen, R. Chen, X. He, X. Zhang, Y. Li, K. Wu, J. Power Sources 342 (2017) 467–475.
- [52] Y. Zhu, W. Liu, X. Zhang, J. He, J. Chen, Y. Wang, T. Cao, Langmuir 29 (2013) 744–749.
- [53] Y. Wen, Y. Zhu, A. Langrock, A. Manivannan, S.H. Ehrman, C. Wang, Small 9 (2013) 2810–2816.
- [54] G.M. Veith, L. Baggetto, R.L. Sacci, R.R. Unocic, W.E. Tenhaeff, J.F. Browning, Chem. Commun. 50 (2014) 3081–3084.

- [55] G. Liu, H.H. Wu, Q. Meng, T. Zhang, D. Sun, X. Jin, D. Guo, N. Wu, X. Liu, J.K. Kim, Nanoscale Horiz. 5 (2020) 150–162.
 [56] J. Shin, T.-H. Kim, Y. Lee, E. Cho, Energy Storage Mater. 25 (2020) 764–781.
 [57] L. Zhao, H.H. Wu, C. Yang, Q. Zhang, G. Zhong, Z. Zheng, H. Chen, J. Wang, K. He, B. Wang, T. Zhu, X.C. Zeng, M. Liu, M.S. Wang, ACS Nano 12 (2018) 12597–12611.
 [58] W. Zhang, R. Du, C. Zhou, S. Pu, B. Han, K. Xia, Q. Gao, J. Wu, Mater. Today Energy 12 (2019) 303–310.
- [59] X. Xia, S. Deng, D. Xie, Y. Wang, S. Feng, J. Wu, J. Tu, J. Mater. Chem. A 6 (2018) 15546-15552.
- 13540-13552.
 [60] Y.-C. Zhang, Y. You, S. Xin, Y.-X. Yin, J. Zhang, P. Wang, X.-S. Zheng, F.-F. Cao, Y.-G. Guo, Nano Energy 25 (2016) 120-127.
 [61] H.H. Wu, H. Huang, J. Zhong, Y. Song, Q.B. Zhang, X.C. Zeng, Nanoscale 11 (2019) 12210-12219.